

# A SPECT-based method for dynamic imaging of the glymphatic system in rats

Björn Sigurdsson<sup>1,\*</sup> , Natalie L Hauglund<sup>1,\*</sup> ,  
Tuomas O Lilius<sup>1,2,3,4</sup>, Frida L-H Mogensen<sup>1,5,6</sup> ,  
Kristian N Mortensen<sup>1</sup>, Natalie Beschorner<sup>1</sup>, Laura Klinger<sup>1</sup>,  
Simone L Bærentzen<sup>7,8</sup>, Marko P Rosenholm<sup>1</sup> ,  
Vladimir Shalgunov<sup>9</sup>, Matthias Herth<sup>9,10</sup>, Yuki Mori<sup>1</sup> and  
Maiken Nedergaard<sup>1,11</sup>

Journal of Cerebral Blood Flow & Metabolism  
0(0) 1–13  
© The Author(s) 2023  
Article reuse guidelines:  
sagepub.com/journals-permissions  
DOI: 10.1177/0271678X231156982  
journals.sagepub.com/home/jcbfm



## Abstract

The glymphatic system is a brain-wide waste drainage system that promotes cerebrospinal fluid circulation through the brain to remove waste metabolites. Currently, the most common methods for assessing glymphatic function are *ex vivo* fluorescence microscopy of brain slices, macroscopic cortical imaging, and MRI. While all these methods have been crucial for expanding our understanding of the glymphatic system, new techniques are required to overcome their specific drawbacks. Here, we evaluate SPECT/CT imaging as a tool to assess glymphatic function in different anesthesia-induced brain states using two radiolabeled tracers, [<sup>111</sup>In]-DTPA and [<sup>99m</sup>Tc]-NanoScan. Using SPECT, we confirmed the existence of brain state-dependent differences in glymphatic flow and we show brain state-dependent differences of CSF flow kinetics and CSF egress to the lymph nodes. We compare SPECT and MRI for imaging glymphatic flow and find that the two imaging modalities show the same overall pattern of CSF flow, but that SPECT was specific across a greater range of tracer concentrations than MRI. Overall, we find that SPECT imaging is a promising tool for imaging the glymphatic system, and that qualities such as high sensitivity and the variety of available tracers make SPECT imaging a good alternative for glymphatic research.

## Keywords

Waste clearance, rat brain, cerebrospinal fluid dynamics, [<sup>111</sup>In]-DTPA, lymph nodes

Received 10 August 2022; Revised 17 November 2022; Accepted 7 December 2022

## Introduction

Neuroimaging of brain perfusion and receptor binding using single photon emission computed tomography (SPECT) has been widely used in the study of diseases

such as dementias, cancer, neuropsychiatric disorders, and vascular diseases.<sup>1–6</sup> However, the use of SPECT for imaging the glymphatic system has so far been limited.<sup>7</sup>

<sup>1</sup>Center for Translational Neuromedicine, University of Copenhagen, Denmark

<sup>2</sup>INDIVIDRUG Research Program, University of Helsinki, Finland

<sup>3</sup>Department of Pharmacology, University of Helsinki, Finland

<sup>4</sup>Department of Emergency Medicine and Services, Helsinki University Hospital and University of Helsinki, Finland

<sup>5</sup>Neuro-Immunology Group, Department of Cancer Research, Luxembourg Institute of Health, Luxembourg, Luxembourg

<sup>6</sup>Doctoral School of Science and Technology, University of Luxembourg, Esch-sur-Alzette, Luxembourg

<sup>7</sup>Translational Neuropsychiatry Unit, Department of Clinical Medicine, Aarhus University, Aarhus, Denmark

<sup>8</sup>Department of Nuclear Medicine and PET Center, Aarhus University Hospital, Aarhus, Denmark

<sup>9</sup>Department of Drug Design and Pharmacology, University of Copenhagen, Denmark

<sup>10</sup>Department of Clinical Physiology, Copenhagen University Hospital, Denmark

<sup>11</sup>Center for Translational Neuromedicine, University of Rochester Medical Center, USA

\*These authors contributed equally to the work.

## Corresponding author:

Maiken Nedergaard, University of Rochester Medical Center, School of Medicine and Dentistry, 601 Elmwood Ave, Box 645, Rochester, NY 14642, USA.

Email: Maiken\_Nedergaard@URMC.Rochester.edu

The glymphatic system is a cerebrospinal fluid (CSF)-mediated waste and solute drainage system initially discovered in the rodent brain<sup>8–13</sup> and later described in the non-human primate brain<sup>14,15</sup> and human brain.<sup>16–20</sup> The glymphatic system is a fluid transport system that includes (1) CSF flow facilitated by arterial pulsations along the periarterial spaces of leptomeningeal arteries followed by (2) CSF influx into the interstitial space and subsequent CSF-interstitial fluid (ISF) mixing within the neuropil, and eventually, (3) drainage of fluid via the venous perivascular sites with additional drainage to arachnoid granulations, cranial and spinal nerves, as well as meningeal and cervical lymphatic vessels.<sup>8,21–26</sup> The polarized transport of CSF and interstitial fluid produces an efficient way to clear the brain of endogenous molecules, such as amyloid- $\beta$ , and metabolites, such as lactate.<sup>8,27</sup>

SPECT imaging relies on the detection of gamma-rays emitted from a single-photon-emitting radionuclide<sup>28</sup> and is used in both clinical and preclinical settings. Similar to magnetic resonance imaging (MRI), SPECT combined with computed tomography (CT) can acquire dynamic 3D images of tracer distribution but with higher specificity and sensitivity than MRI. Here, we compared SPECT imaging with MR imaging for assessing glymphatic function by imaging tracer distribution in rats under different anesthetic regimens, and we used SPECT/CT for investigating CSF flow velocity and egress to lymph nodes.

## Methods

### Animals

All procedures were approved by the Danish Animal Experiments Inspectorate and carried out at the Center for Translational Neuromedicine, University of Copenhagen, in accordance with the European Directive 2010/63/EU under the license 2015-15-0201-00535 and followed the ARRIVE guidelines. Two separate groups of 10–14 weeks old male Sprague-Dawley rats ( $n = 14$ , 200–250 g, Charles River, Salzburg, Germany) were used for [<sup>111</sup>In]-DTPA (diethylenetriamine penta-acetic acid) and MRI experiments. 10–14 weeks old female Sprague-Dawley rats ( $n = 14$ , 200–300 g, Janvier Laboratories) were used for the experiments with [<sup>99m</sup>Tc]-NanoScan. Biological sex does not influence glymphatic flow in mice,<sup>29</sup> and the different sex of the rats in this study is therefore not likely to alter the results. Rats were housed in pairs in individually ventilated plastic cages with ad-libitum access to water and standard rodent chow in temperature-controlled rooms with a 12 h light/dark cycle. All experiments were performed during the light phase.

### Animal preparation

The cisterna magna cannulation procedure was performed as previously described with minor modifications.<sup>30</sup> Rats were anesthetized with either a combination of subcutaneous ketamine (100 mg/kg) and dexmedetomidine (0.5 mg/kg) (K/D) or 3% isoflurane. After verification of loss of response to toe pinch, animals were placed in a stereotaxic frame with the neck slightly flexed (30–40°). The atlanto-occipital membrane overlying the cisterna magna was exposed and a 30G needle connected to a 4-cm long PE10 tubing (Scandidact) was carefully inserted into the intrathecal space. The catheter was fixed with cyanoacrylate glue (Loctite) cured with glue accelerator followed by application of dental cement. Afterwards, rats were transferred to the imaging bed. Rats anesthetized with K/D did not receive extra anesthetics whereas isoflurane-anesthetized rats were maintained under 1.5–1.7% isoflurane anesthesia with 50:50 air and oxygen gases throughout the experiments. Body temperature and respiration were maintained and monitored throughout the experiment.

### Radioactive tracers

For glymphatic flow studies using SPECT, [<sup>111</sup>In]-DTPA (Curium Pharma, 545.3 Da, 37 MBq/mL at activity reference time, 0.1 mg/mL pentetic acid, DTPA) in a sterile injectable water solution (pH 7.2) containing sodium chloride (7.1 mg/mL), disodium phosphate dodecahydrate (5.0 mg/mL), calcium chloride dihydrate (37.4  $\mu$ g/mL), sodium hydroxide (0.7 mg/mL) and hydrochloric acid (0.2 M, 0.7 mg/mL), was used directly and within 5 days. For analysis of flow to the lymph nodes, [<sup>99m</sup>Tc]-NanoScan (The Department of Clinical Physiology, Nuclear Medicine and PET, Rigshospitalet, 66.5 kDa, 1000 MBq/mL at activity reference time) was used.

### SPECT/CT acquisition

The VECTor4CT (MILabs, Utrecht, Netherlands) system with a high energy ultra-high resolution (voxel size: 0.8  $\times$  0.8  $\times$  0.8 mm) rat clustered multi-pinhole collimator (HE-UHR-RM, 1.8 mm pinhole diameter) was used for both CT and SPECT acquisition. A 100  $\mu$ L Hamilton microsyringe (Sigma Aldrich, Denmark) with 60  $\mu$ L [<sup>111</sup>In]-DTPA or [<sup>99m</sup>Tc]-NanoScan was connected to the cisterna magna catheter. A full-body CT scan was performed followed by a SPECT acquisition covering the brain and upper spinal cord. Infusion of 40  $\mu$ L [<sup>111</sup>In]-DTPA or [<sup>99m</sup>Tc]-NanoScan was carried out over the first 20 minutes of the scan, followed by 160 minutes of post-injection SPECT acquisition. The full-body CT scan was

acquired with 55 kV tube voltage, 75 ms exposure time,  $\times 11$  binning and 360 projections with a step angle of 0.75 degrees over 9 minutes. The SPECT acquisition was performed over 4 cycles, the first cycle consisting of 10 frames with 3 minutes per frame, and the following 3 cycles consisting of 5 frames with 10 minutes per frame resulting in a total scan time of 180 minutes. Head scans were acquired with 30 bed positions and the detection peak energy was set to 1200 keV. Scatter and CT-based non-uniform attenuation correction were performed, and the images were reconstructed using a Similarity-Regulated Ordered Subsets Estimation Maximization (SROSEM) with a voxel size of 0.8 mm for  $^{111}\text{In}$  and 0.6 mm for  $^{99\text{m}}\text{Tc}$ , and 5 iterations. A 0.8 FWHM (mm) gaussian filter was added post reconstruction. For reconstruction of  $^{111}\text{In}$  scans, only decays at the  $^{111}\text{In}$  photopeaks (176 ( $\pm 11\%$ ) keV and 277.2 ( $\pm 20\%$ ), background at 4% and 10% outside each photopeak window) were used for the reconstruction.  $^{99\text{m}}\text{Tc}$  scans were reconstructed with a photopeak window centered around 140 keV with 20% width. The injected dose was calculated for each rat by measuring the activity of the vial with a VIK-202 dose calibrator (Comer, Joure, Netherlands) before and after tracer injection and subtracting background activity and the activity left in the tubing after the scan. All injected doses and scans were decay corrected to the start of the first scan and quantified.

### MRI acquisition

MRI was carried out on a 9.4 T magnet (Bruker BioSpec 94/30 USR) interfaced to a Bruker AVANCE III console, controlled by Paravision software (Bruker, ver 5.1) and using an 86 mm volume RF-transmit coil and a 4-channel phased array RF receiver coil (Bruker). Rats were placed in the prone position in the scanner with teeth fixed in a bite-bar and a 100  $\mu\text{L}$  Hamilton micro-syringe with Gd-DTPA (BioPAL Inc.) diluted to 12.5 mM in saline was connected to the cisterna magna catheter. Respiration rate and rectal temperature were monitored throughout the experiment. The quantitative dynamic contrast-enhanced MRI method was adapted from previous work.<sup>31</sup> First, a double angle experiment was carried out to measure B1+-field inhomogeneity, using rapid acquisition with relaxation enhancement (RARE) sequence (echo time (TE): 22 ms, repetition time (TR): 10 s, RARE factor: 4, 50 horizontal slices, matrix:  $128 \times 128$ , in-plane resolution:  $0.24 \times 0.24$  mm, slice thickness: 0.4 mm; slice gap: 0.2 mm; flip angle (FA):  $70^\circ$  and  $140^\circ$ ). A pre-contrast T1-map was measured using the variable flip angle 3D-spoiled gradient method (VFA-SPGR) (TE: 4 ms, TR: 15 ms, matrix:  $128 \times 128 \times 128$ , 3D resolution:  $0.24 \times 0.24 \times 0.26$  mm, FA: 2, 5, 10, 15, 20, and  $30^\circ$ ). Then, a series of

SPGR-images were acquired (FA:  $15^\circ$ , otherwise same parameters as above) consisting of three pre-contrast baseline images, followed by the infusion of 40  $\mu\text{L}$  Gd-DTPA solution over 20 min and the acquisition of 42–45 post-contrast images, continuing 180–200 min after contrast infusion initiation.

### Ex vivo fluorescence imaging of brain slices

A rat was anesthetized with K/D, and 60  $\mu\text{L}$  FITC dextran (3 kDa; ThermoFisher) was injected into the cisterna magna over 20 minutes. 30 minutes after the end of the injection, the rat was euthanized by cervical dislocation and the brain was immediately dissected and placed in PFA overnight. The following day the brain was cut in 100  $\mu\text{m}$  thick coronal slices on a vibratome (VT1200S, Leica Biosystems), and slices were mounted on glass slides and imaged on a Nikon Eclipse NI-E epifluorescence microscope using NIS Elements software. Multichannel whole-slice images were generated at  $4 \times$  magnification with emission filters for fluorescein isothiocyanate (FITC).

### Data analysis

CT and SPECT data was reconstructed with MiLabs reconstruction software. SPECT images were normalized to the injected dose of radioactivity as measured by a scintillation counter, converting them to units of percent injected dose per cubic centimeter (%ID/cc). CT images were motion corrected, along with their respective SPECT images, and rigidly co-registered to an in-house T2 weighted MRI rat atlas using Advanced Normalization Tools (ANTs).<sup>32</sup> Regions of interests (ROIs) were drawn on the MRI atlas using ITK-SNAP v3.8.0 and time activity curves were extracted using Python 3.9. The co-registered and normalized SPECT images were averaged according to the anesthesia regimen and time of acquisition for display purposes. The anatomical location of the lymph nodes according to Van den Broeck et al.<sup>33</sup> was used to identify the lymph nodes analyzed. The superficial parotid lymph nodes and deep cervical lymph nodes were analyzed as one entity because their proximity and high signal often made them indistinguishable.

SPGR-MRI data was first motion corrected using ANTs and processed according to a previously published method to convert them to mM units<sup>31</sup> and then normalized to the total amount of Gd-DTPA injected, producing values in units of percent of total injected dose per cubic centimeter (%ID/cc). The T2 weighted MRI rat atlas was registered non-linearly to each experiment along with the ROIs used for the SPECT data and time activity curves were extracted using Python 3.9. MR images were co-registered and



averaged according to their anesthesia regimen and time of acquisition. Data acquisition and analysis was performed un-blinded.

### Statistical analysis

Data in line plots are expressed as the mean  $\pm$  standard deviation (SD). Data in bar plots are expressed as the mean  $\pm$  SD along with a point for each experiment. The Anderson-Darling test was used to test for normality. A two-sided independent t-test was used for group comparisons of normally distributed data and the non-parametric Mann Whitney U test for non-normally distributed data (Python 3.9, statsmodels 0.13.1, SciPy 1.7.3). Threshold for significance was considered to be  $p < 0.05$ .

## Results

### Comparison of SPECT with MRI and ex vivo fluorescence

We first evaluated if SPECT imaging shows the same tracer distribution pattern as MRI following infusion of tracer into the cisterna magna. Rats were anesthetized with a combination of ketamine and dexmedetomidine (K/D), and consecutive images of CSF tracer distribution were acquired with SPECT or MRI over

a period of 180 minutes. Separate cohorts of rats were used for SPECT and MRI experiments and included 5 rats for SPECT experiments and 4 rats for MRI experiments. *Ex vivo* fluorescence imaging of brain sections 30 minutes after infusion of 3 kDa FITC dextran was performed on one rat for comparison as seen in Figure 1(a). The type and size of CSF tracers affects their distribution,<sup>8</sup> therefore we used DTPA for both the SPECT and MRI imaging. DTPA labelled with <sup>111</sup>In ([<sup>111</sup>In]-DTPA, 545 Da) was used for SPECT and DTPA labelled with gadolinium (Gd-DTPA, 575 Da) was used for MRI. All three imaging modalities showed the largest tracer accumulation in the ventral brain areas, while less tracer reached the deeper structures and dorsal surface (Figure 1(b)). *Ex vivo* imaging of brain slices showed accumulation of tracer in the lateral cortex as well as around the induseum griseum. However, tracer accumulation in these regions was not detected with MRI or SPECT. The higher tracer accumulation observed in the *ex vivo* images may be due to CSF influx caused by vessel constriction during spreading depolarization<sup>34</sup> which has been reported in animals following cerebral edema after cardiac arrest.<sup>25,35</sup> We further evaluated tracer distribution with SPECT and MRI over time (Figure 1(c)). Visual comparison of images acquired with SPECT and MRI showed the same overall pattern and

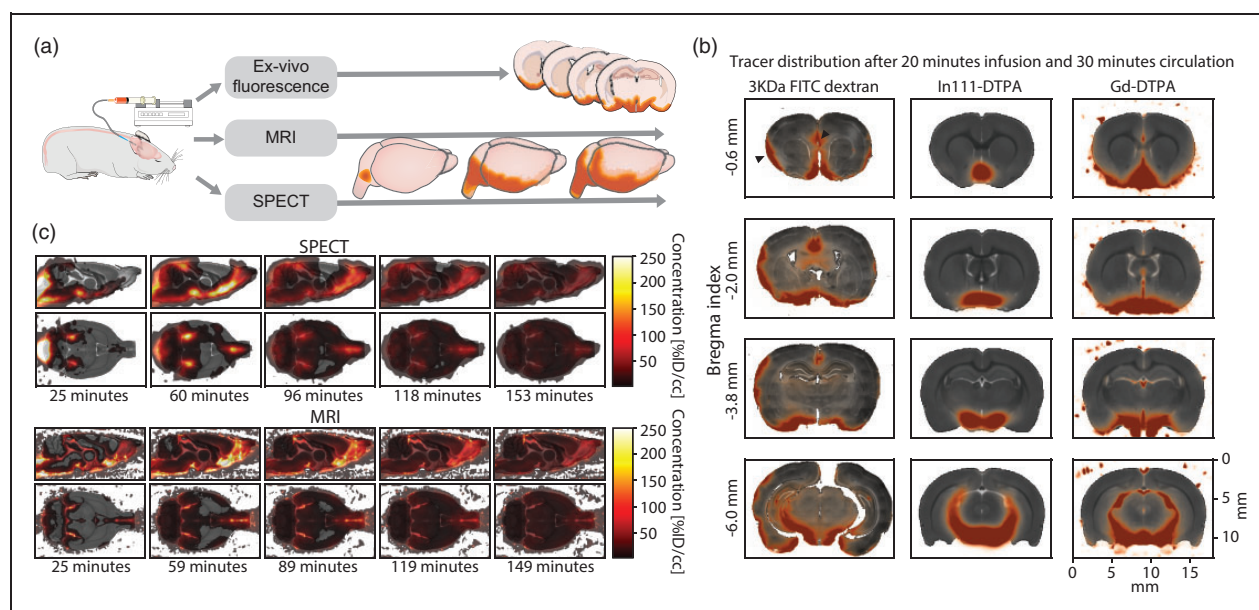


**Figure 1.** Optical, MRI and SPECT imaging depict a similar pattern of CSF tracer influx. (a) Experiment diagram showing the infusion of tracer into the cisterna magna of a rat, the imaging methods, and the respective data they produce. (b) Coronal slices of the rat brain 30 minutes after infusion of tracer to the cisterna magna. Left column: 3 kDa FITC dextran distribution in the brain imaged *ex vivo* using a fluorescence microscope (black arrows indicate tracer influx to the lateral cortex and the induseum griseum). Middle column: [<sup>111</sup>In]-DTPA distribution imaged *in vivo* using a SPECT scanner (average of 5 images). Right column: Gd-DTPA distribution imaged *in vivo* using a 9.4 T MRI (average of 4 images). (c) Distribution of DTPA in the rat brain over time in a sagittal and a horizontal plane as imaged with SPECT (top) and MRI (bottom). Background in both is an MRI rat template.

dynamics of tracer influx, with tracer spreading mainly to the ventral surface of the brain at the early time points and increasing penetration into the brain parenchyma over time. In the brain areas with high tracer accumulation, tracer distribution was characterized by an influx phase that spanned the first 60 minutes and was followed by a clearance phase with gradual decrease in tracer signal during the remaining acquisition. In areas with lower tracer accumulation, a slow, gradual build-up of tracer spanned the first 120 minutes and was followed by a slow decrease. In conclusion, all three imaging modalities showed approximately the same tracer accumulation following 30 minutes of tracer circulation, and SPECT and MRI showed a comparable tracer distribution pattern over a 150-minute period.

### Comparison of SPECT and MRI for glymphatic imaging in different brain states

Glymphatic CSF flow is dependent on brain state with increased CSF entry to the brain during sleep or certain types of anesthesia such as ketamine/xylazine (K/X) and ketamine/dexmedetomidine (K/D).<sup>36–39</sup> We therefore next compared the ability of SPECT and MRI to dynamically assess glymphatic tracer distribution

under either isoflurane or K/D, which have previously been shown to inhibit and increase glymphatic influx, respectively<sup>36,39</sup> (Figure 2(a)). Rectal temperature and respiration were monitored throughout the scans and confirmed different physiological parameters between the two anesthesia groups (Supplementary Figure 1). Regions of interest were placed in the cortex, striatum, and hippocampus in both hemispheres to compare tracer penetrance between the two imaging modalities (Figure 2(b)). Comparison of tracer dynamics over time in the two groups that were detected with both SPECT and MRI (Figure 2(c) and Supplementary Movie 1). Tracer distribution within the CSF compartment was faster in rats anesthetized with isoflurane. At 20 minutes after tracer infusion, isoflurane-anesthetized rats showed substantial tracer spread via the ventral CSF compartments to the nasal area and the cervical spine, while tracer in K/D-anesthetized rats was still localized close to the injection site. In accordance with the notion that glymphatic influx is enhanced by K/D,<sup>38,39</sup> tracer penetration into the brain was larger in rats anesthetized with K/D than with isoflurane. Time activity curves for isoflurane and K/D appeared highly similar between SPECT and MRI for the cortex, hippocampus, and striatum (Figure 2(d) to (f)).

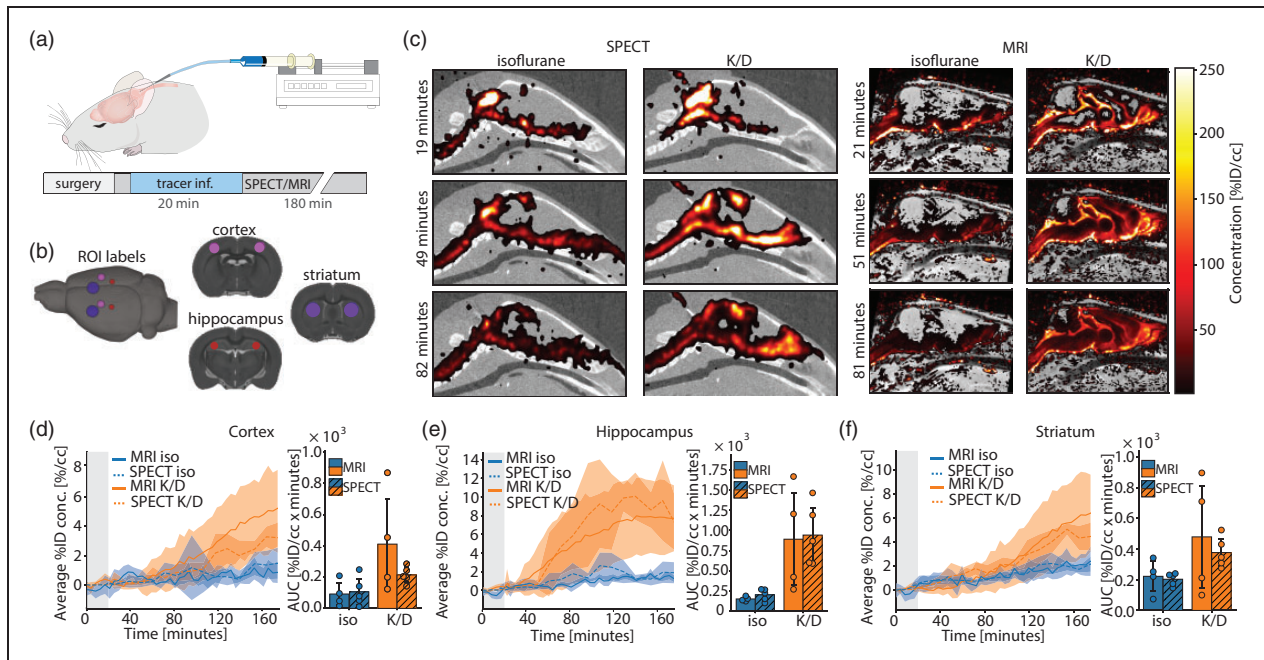


**Figure 2.** Dynamic imaging confirms agreement on tracer distribution between MRI and SPECT. (a) Diagram of the experimental setup. (b) ROI labels used for the analysis. (c) Sagittal view of the distribution of  $[^{111}\text{In}]\text{-DTPA}$  over time in the rat brain under isoflurane or K/D imaged by SPECT (left) and distribution of Gd-DTPA imaged by MRI (right). Lower threshold is at 2%ID/cc for both. Time-activity curves (left) and analysis of area under the curve (right) in the rat cortex (d), in the hippocampus (e), in the striatum (f) under K/D or isoflurane as imaged by SPECT or MRI. The grey shaded area shows the infusion time. The colored shaded areas on the line plots and the error on the bar plots are the standard deviation. No significant difference was found between MRI and SPECT in (d), (e), and (f) using a two-sided independent t-test. K/D: ketamine-dexmedetomidine; Iso: isoflurane.

While ROIs in the parenchyma showed good agreement between SPECT and MRI, we noted that if the ROIs included areas of very high tracer concentration, such as the cisterna magna, time-activity curves were different between the two imaging modalities. This was evident when comparing an ROI that included the entire intracranial space, which comprises both brain and CSF spaces (Figure 3). Here, SPECT showed a sharp increase during the infusion, corresponding to tracer entering the CSF space, for both anesthesia groups. After the end of the tracer infusion, rats in the isoflurane group exhibited a fast decrease in tracer concentration, while rats in the K/D group remained stable before gradually decreasing. Analysis of the same ROI in images acquired with MRI did not show the same pattern, but instead a slow increase followed by a slow decrease for both anesthetics, with higher tracer content in the K/D group. Because the intracranial space ROI includes the injection site, we would expect the time activity curves of the two anesthetics to be highly similar for the first frame, which was indeed what was seen for the SPECT experiments. However, this was not the case for the MRI time activity curves, which indicates that MRI in this setup was less specific to variances in tracer concentrations than SPECT. Overall, we confirm prior studies showing that isoflurane and K/D have opposing effects on the glymphatic system.<sup>36,38</sup> Furthermore, SPECT was capable of detecting brain state-dependent differences in glymphatic flow and tracer distribution across large differences in tracer concentrations, making it a suitable alternative to MRI for glymphatic system imaging.

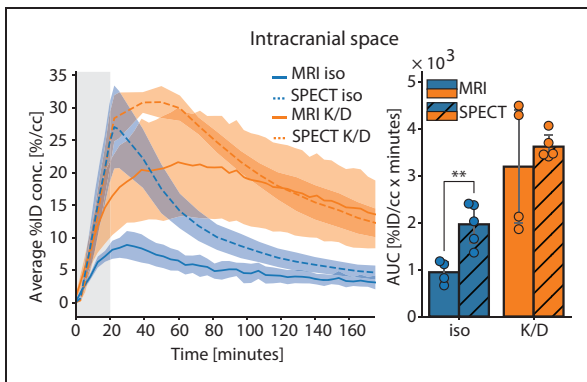


**Figure 3.** MRI measures less tracer in the intracranial space than SPECT at first but converges with SPECT measurements as time progresses. Mean tracer concentration over time in the rat intracranial space under K/D or isoflurane anesthesia as imaged by SPECT or MRI.  $n = 4-5$ . The grey shaded area depicts time when the pump is on. The colored shaded areas on the line plots and the error on the bar plots are the standard deviation. KD: ketamine-dexmedetomidine; Iso: isoflurane; AUC: area under the curve; ID: injected dose. Two-sided independent t-test, \*\* =  $P < 0.001$ .

### CSF flow velocity measurements using SPECT

An advantage of dynamic 3D imaging is that it allows for velocity measurements of tracer distribution. We modeled the CSF space at the ventral surface of the rat brain as a simple one-dimensional tube lying in the posterior-anterior direction and split the tube into regions of consecutive 0.016 mm thick discs perpendicular to the average direction of the flow (Figure 4(a)). The tracer concentration inside the tube was then summed in every region and at every point in time to create the concentration matrix  $C_{x,t}$  and fit the flow of concentration equation below, where  $v$  is the average velocity of the tracer in posterior-anterior direction.

$$\frac{d}{dt} C_{x,t} = -v \cdot \frac{d}{dx} C_{x,t}$$

We approximated the time and space concentration derivative of every region and time point by subtracting the concentration of the preceding region and time point. The slope of the best fitting line to every space and time derivative pair is the average speed of the tracer through the tube (Figure 4(b)). Using this method, we found that the average speed of the tracer flowing along the ventral surface of the rat brain was 1.7 times faster in rats anesthetized with isoflurane than K/D (0.135 cm/minute for K/D and 0.081 cm/minute for isoflurane, Figure 4(c)).

We estimated the time of arrival in several brain regions and efflux routes by calculating the time at which the tracer concentration had reached 10% of the maximum concentration in each region (Figure 4(d) and (e)). As expected due to the greater speed, the time of arrival was lower under isoflurane than K/D in most brain regions as well as in the cervical spine and olfactory nerve. However, the time of arrival was not significantly different in the deep brain regions of cortex and hippocampus indicating that other parameters are likely to govern CSF flow speed within the deep tissue of the brain. Overall, we found that CSF flow speed along the ventral surface, as well as tracer arrival to all analyzed areas except the cortex and hippocampus was significantly faster under isoflurane anesthesia.

### CSF egress to lymph nodes under different anesthetics

To further evaluate SPECT as a method to investigate the glymphatic pathways, we utilized the SPECT tracer [ $^{99m}\text{Tc}$ ]-human serum albumin nanocolloid (NanoScan) that targets lymph tissue.<sup>40</sup> [ $^{111}\text{In}$ ]-DTPA quickly passes through the lymph vessels or along nerve sheaths to the peripheral blood stream which makes it difficult to detect clearance to the lymph nodes.<sup>41</sup> NanoScan is



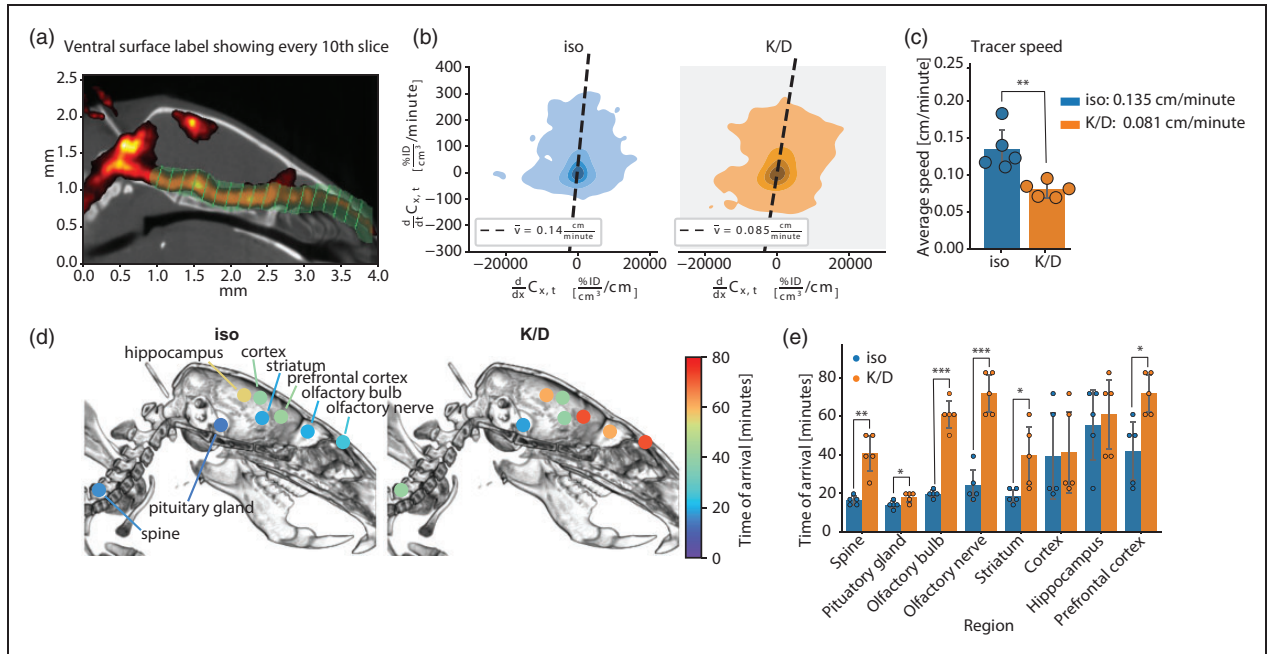


**Figure 4.** Tracer in CSF spaces flows faster under isoflurane than under K/D. (a) Example of regions of interest used to calculate the speed of tracer across the ventral surface of the rat brain. Each region is a 0.16 mm thick disk positioned perpendicular to the direction of the flow. (b) Kernel density plots of the time and space derivatives of tracer concentration in the ventral surface of the rat brain and the best fitting line. Each level (including white) contains 20% of the data points. Supplemental figure 5 contains linear regression fit for each experiment. (c) Bar plots showing a significant difference in the flow speed of tracer across the ventral surface of the rat brain under K/D and isoflurane. (d) Diagram of the rat head and spine showing the time of arrival in several regions. Time of arrival is defined as when the concentration in a region reaches 10% of the maximum recorded concentration in the region. (e) Comparison of the tracer arrival times for K/D and isoflurane in several regions of the rat brain. Error bars are standard deviation. K/D: ketamine-dexmedetomidine; iso: isoflurane. Two-sided independent t-test, \* =  $P < 0.05$ , \*\* =  $P < 0.01$ , \*\*\* =  $P < 0.001$ .

contained within lymph tissue which makes it optimal for studying CSF drainage to the periphery. Rats were anesthetized with either isoflurane or K/D, and NanoScan was slowly infused into the cisterna magna during imaging (Figure 5(a)). Because of its properties and large size (66.5 kDa), NanoScan should not be able to readily enter the brain parenchyma. This was confirmed by first assessing Nanoscan signal within the deep areas of the brain parenchyma (Figure 5(b)). As expected, tracer to the striatum was very limited, and showed no difference between isoflurane and K/D contrary to the [ $^{111}\text{In}$ ]-DTPA experiment (Figure 5(c)). However, the two anesthetics induced distinct differences in peripheral tracer distribution over time (Figure 5 (d) and Supplementary movies 2 and 3) with a fast filling of lymph nodes in the rats anesthetized with isoflurane compared to rats anesthetized with K/D. Rats anesthetized with K/D had a higher peak tracer concentration in the cervical spinal cord than rats anesthetized with isoflurane (Figure 5(e)). The tracer concentration in the spinal cord remained higher in the K/D group throughout the experiment which may be due to lower CSF flow speed in the K/D group or possible differences in perivascular space volume between the two anesthesia

groups. Isoflurane anesthesia induced a fast shunting of CSF to the superficial parotid/deep cervical lymph nodes that became visible 10 minutes after the beginning of the tracer infusion (Figure 5(f)). On the contrary, rats anesthetized with K/D had less and slower tracer filling of the superficial parotid/deep cervical lymph nodes. For both groups, less tracer was detected in the submandibular lymph nodes than the superficial parotid/deep cervical lymph nodes, but rats anesthetized with isoflurane exhibited significantly higher signal than rats in the K/D group (Figure 4(g)). Rats in the isoflurane group had a faster CSF flow to the nasal area but over time, the two groups ended up at a similar level of tracer (Figure 5(h)). These results indicate that drainage from the CSF compartment to the periphery is faster in isoflurane anesthesia, and that K/D induces a retention of CSF within the CSF compartments and slower drainage to the peripheral lymph nodes.

## Discussion

### Main findings

In this study we show that SPECT/CT is a powerful tool for spatial and temporal imaging of the glymphatic

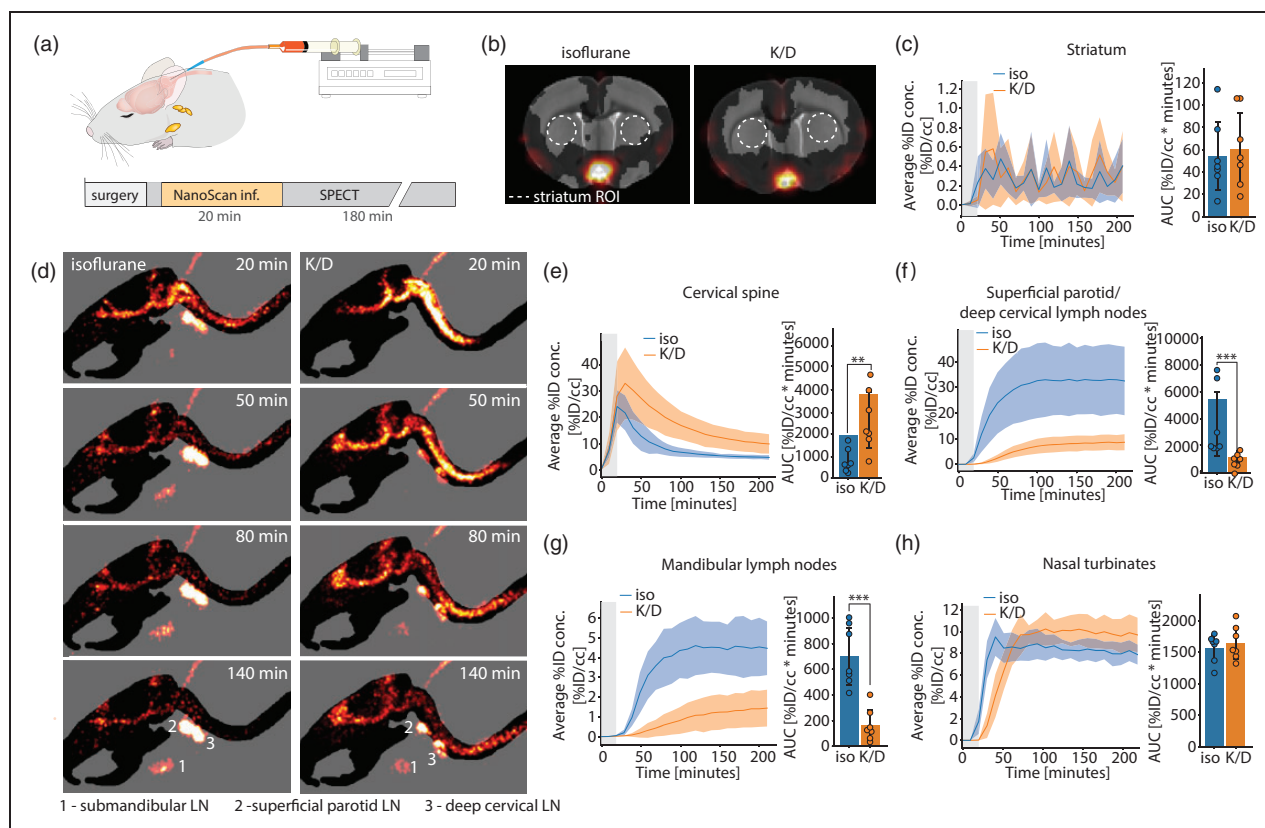


**Figure 5.**  $[^{99m}\text{Tc}]$ -NanoScan injection shows brain-state dependent differences in CSF egress to the lymph nodes. (a) Diagram of the experimental setup. (b) Coronal sections showing limited penetrance of tracer into the brain parenchyma for both isoflurane and K/D groups (each coronal section is an average of all time points from one rat, dashed line shows ROIs used for the striatal analysis). (c) Time-activity curves for tracer flow to the striatum (left) (note y-scale compared to the other graphs) and analysis of area under the curve (right). (d) Sagittal view of representative distribution of NanoScan over time in a rat brain under isoflurane (left) and K/D anesthesia (right). Time-activity curves (left) and analysis of area under the curve (right) in the cervical spine (e), the superficial parotid/deep cervical lymph nodes (f), the submandibular lymph nodes (g), and in the nasal turbinates (h) under K/D and isoflurane as imaged by SPECT ( $n = 7$ ). The grey shaded area depicts time when the pump is on. The colored shaded areas on the line plots and the error on the bar plots are the standard deviation. K/D: ketamine/dexmedetomidine; Iso: isoflurane; AUC: area under the curve; ID: injected dose; LN: lymph nodes. Two-sided independent t-test, \* =  $P < 0.05$ , \*\* =  $P < 0.01$ , \*\*\* =  $P < 0.001$ .

system. Using SPECT, we replicated key features of glymphatic transport previously identified by optical imaging and MRI.<sup>36,39,42</sup> We used SPECT images to calculate the velocity of tracer flow in the ventral CSF compartment and found, for the first time to our knowledge, that CSF flow along the ventral surface of the brain is faster in rats anesthetized with isoflurane than rats anesthetized with K/D (Figure 4). We furthermore used SPECT to investigate CSF shunting from CSF spaces surrounding the brain to lymph nodes by using the SPECT tracer  $[^{99m}\text{Tc}]$ -NanoScan, and showed that isoflurane anesthesia results in faster and larger accumulation of tracer to the submandibular and superficial parotid/deep cervical lymph nodes, while K/D anesthesia induced a more pronounced tracer flow to the cervical spine (Figure 5).

We used previously tested anesthetic regimens that have opposing effects on the glymphatic system to

validate the use of SPECT, and confirmed previous studies showing that K/D promotes glymphatic influx while isoflurane inhibits it<sup>36,38,39</sup> (Figure 2). This difference in flow was detected by both MRI and SPECT (Figure 2). Why more CSF enters the brain under K/D anesthesia than isoflurane is not clear, but it is likely the result of several biological features such as differences in heart rate, neuronal activity patterns, and vascular tone. Dexmedetomidine is known to induce cerebral vasoconstriction while isoflurane is a potent vasodilator.<sup>43,44</sup> Arterial diameter affects the volume of the perivascular space that surrounds it.<sup>45</sup> The perivascular spaces direct CSF flow to the brain, and a smaller perivascular space induced by isoflurane therefore may inhibit CSF flow within the perivascular space.<sup>46</sup> Isoflurane may also affect the permeability of the blood brain barrier (BBB)<sup>47,48</sup> and thereby enhance tracer efflux directly from the periarterial spaces to the



bloodstream. However, since isoflurane impeded CSF flow within the perivascular spaces, the possible alteration in BBB permeability is not likely to markedly affect the tracer distribution.

MRI was less sensitive to areas with high tracer concentration than SPECT (Figure 3). The discrepancy is likely caused by a combination of several technical and biological phenomena, including possible infusion artifacts due to T1/T2 contrast mechanisms in the brain parenchyma, or flow/motion/pulsation artifacts when contrast agent moves away from the injection site through the perivascular spaces. It is important to note, however, that the observed artifact is a result of the imaging parameters used in this specific study and would not necessarily apply to other MRI studies using different imaging parameters. Tuning different parameters and/or decreasing tracer concentration could likely improve or correct the quantification of areas with high tracer content. On another note, tracer concentration optimization could introduce other challenges such as difficulties with detecting tracer within the deeper parts of the brain parenchyma, and imaging parameters and tracer concentration should therefore always be chosen based on the goal of the study. This finding also highlights the important advantage of SPECT imaging that concentration is measured directly by counting emissions of radionuclide unlike MRI, which estimates contrast agent concentration by measuring its effect on surrounding hydrogen protons.<sup>49</sup>

We used SPECT to measure flow velocities of CSF and found that isoflurane anesthesia results in 1.7 times faster CSF flow velocity in the ventral CSF compartment compared to K/D anesthesia. The average velocity of 0.081 cm/minute we measured under K/D is very close to the average flow speed of 0.112 cm/minute that has previously been reported by Mestre et al. who looked at flow in the perivascular space of mice under K/X with two-photon microscopy.<sup>50</sup> Another study used dynamic contrast-enhanced MRI to study CSF flow speed in rats and reported a slower speed of ~0.0012 cm/minute.<sup>51</sup> The difference in speed might be because more of the CSF compartment was included in the study, whereby potential low-speed areas would decrease the average flow speed. Interestingly, the same study found that a rat model of cerebral amyloid angiopathy had faster CSF flow speed but lower glymphatic influx than wildtype control rats. This fits with the higher flow speed but lower brain influx we see under isoflurane, and points to the interesting possibility that CSF flow speed potentially could have a direct effect on glymphatic influx. As the flow of tracer through the ventral CSF compartment is relatively fast, and the tracer infusion is slow (over the course of 20 minutes), the velocity measurements in this study are performed while the injection is still ongoing. It is

therefore possible that the velocity measurements are confounded by the injection pressure from the pump. However, tracer flow to the spine and olfactory bulb was also several times slower in rats anesthetized with K/D, with times of arrival 20 and 40 minutes after those of rats anesthetized with isoflurane, respectively, which is after the pump has been turned off. Either way, the findings provide evidence for differences in flow between the two anesthetics. One possible reason for this difference may be the vasodilation induced by isoflurane anesthesia, which leads to a constriction of the CSF space and thus a higher pressure. On the contrary, vasoconstriction induced by K/D result in an increased volume of perivascular spaces and thereby less flow resistance (Supplemental figure 4). Another possibility is different rates of CSF production between the two anesthetics. Isoflurane increases the rate of CSF production compared to wakefulness and K/X anesthesia,<sup>52</sup> and an increased CSF production rate would most likely increase flow velocity throughout the CSF spaces of the brain.

To study CSF dynamics with SPECT, we used the tracer [<sup>111</sup>In]-DTPA that is clinically used for the diagnostics of CSF leaks and is excreted via the kidneys.<sup>53,54</sup> Unlike SPECT- and PET tracers traditionally used for receptor-binding studies, glymphatic flow tracers should not be blood-brain barrier permeable. Blood-brain barrier permeability would result in diffusion through perivascular spaces into the brain bypassing the glymphatic system. Another key property of a good glymphatic tracer is that it should not be taken up by or bound to cells or other material within the brain, as this could slow down or abolish flow within the brain and efflux from the brain to the periphery.<sup>55</sup> In this study, we used the SPECT tracer [<sup>99m</sup>Tc]-NanoScan that binds to lymphatic tissue to specifically study the clearance pathway of CSF to lymph nodes under K/D or isoflurane. CSF flow to the brain or to the lymph nodes has previously been observed to exhibit an opposing relationship with more tracer shunting to the lymph nodes when glymphatic influx is low.<sup>35,56</sup> Our study confirms this relationship and finds that CSF flow to the lymph nodes is limited when tracer inflow to the brain is high (K/D), and that flow to the lymph nodes is faster and more pronounced when brain inflow is low (isoflurane). This inverse relationship is interesting because it suggests a tight link between cerebral and peripheral fluid flow. The same inverse relationship has also been observed in a study comparing awake mice and mice anesthetized with a mix of ketamine and medetomidine, which suggest that it is not only an effect of anesthesia.<sup>35</sup> Obstruction of the meningeal lymph vessels decreases glymphatic influx, while meningeal lymphangiogenesis affects glymphatic influx.<sup>24,57</sup> It is therefore also of

interest if manipulations of the peripheral lymphatic system might affect glymphatic flow and potentially be used to enhance brain clearance. It is, however, important to keep in mind that the tracer egress to the lymph nodes observed in this study is not clearance of tracer from the brain, but from the CSF spaces around the brain. An important future study will be to investigate the effect of anesthesia on clearance of tracer that has been injected directly into the brain parenchyma. A limitation of this study is that a direct correlation between brain inflow and clearance to the lymph nodes was not possible as [ $^{111}\text{In}$ ]-DTPA could not be visualized in the lymph nodes while [ $^{99\text{m}}\text{Tc}$ ]-NanoScan did not enter the brain. Therefore, our results suggest an opposite relationship between inflow and lymph node clearance but to directly show this relationship, a tracer that can be visualized in both brain parenchyma and lymph nodes would be needed. Another limitation is that for some animals, we were not able to clearly differentiate between lymph nodes situated close to each other, and we therefore analyzed the superficial parotid and the deep cervical lymph nodes as one entity. In future studies, a fluorescent tracer, such as Evans blue, that targets lymph nodes could be used together with post-hoc lymph node dissection to potentially help with the identification and analysis.

Another recent study injected the lymphatic SPECT tracer [ $^{64}\text{Cu}$ ]-Albumin into the spinal cord of mice and studied the clearance of CSF from spinal cord to lymph nodes during isoflurane anesthesia.<sup>41</sup> This study also found robust clearance to lymph nodes that was visible after an hour (scans in this study were performed after 9 minutes, 1 hour, 2 hours and increasing intervals up to 24 hours following injection). Interestingly, this study showed the greatest tracer accumulation in the submandibular area, while the area of the superficial parotid and deep cervical lymph nodes had less signal, which is opposite of our results. This indicates that clearance routes for CSF in the spine and for CSF around the brain might favor different lymphatic drainage pathways. An MRI study also investigated the flow of CSF tracer to the brain and lymph nodes in mice, and also found clearance of CSF to the submandibular and deep cervical lymph nodes.<sup>58</sup> That study also tested different anesthetic regimens (isoflurane and K/X), and reported higher brain inflow in mice anesthetized with K/X which corresponds with ours and previous findings. However, assessment of differences in egress to lymph nodes under the two anesthetics was not possible for them due to the motion artifacts in the neck region induced by isoflurane.

### Technical considerations

Fluorescence microscopy of *ex vivo* rodent brain slices has been widely used to observe the distribution of fluorescent tracer in the brain following tracer infusion into the cisterna magna.<sup>8,24,59,60</sup> However, postmortem analysis of brain tissue for glymphatic studies introduces potential confounders due to the collapse of perivascular space integrity post-death, accelerating influx of CSF.<sup>25,35,50</sup> Also, spatial and temporal information about influx and efflux kinetics are lost as each experiment is limited to one specific time point. *In vivo* fluorescence imaging of glymphatic influx in alive animals can be obtained with 2-photon imaging and transcranial macroscopic imaging,<sup>8,61</sup> but have the drawbacks that the field of view is limited and restricted to the cortical surface. Several studies have measured *in vivo* concentrations of CSF tracers continuously over several hours in the rodent brain using dynamic contrast enhanced MRI (DCE-MRI),<sup>9,12,42,60</sup> which overcomes many of the drawbacks of fluorescence imaging. However, quantitative DCE-MRI have potential drawbacks such as local movement artifacts (i.e. if tissue shrinks/grows), flow-related artifacts, and changes in tissue T1 (e.g. due to dehydration or vasodilation/-constriction), which can all result in imprecise or incorrect measurements.<sup>62</sup> While sophisticated image alignment algorithms can correct for small head movements because of the rigidity of the brain and skull,<sup>32</sup> movement of organs in the rest of the body is less restricted which can make quantitative DCE-MRI challenging for multi-session or awake imaging. However, recent advances in glymphatic system MR imaging have removed the need for a pre-contrast baseline image making it more robust to movement.<sup>58</sup> Contrary to MRI, SPECT signal is trivially quantitative and linear with concentration of tracer in the tissue over a large concentration range when corrected for photon attenuation and scattering. This also has the benefit that analysis of SPECT data does not require a baseline image, which makes it less sensitive to movement artifacts. Therefore, SPECT is suitable for imaging awake rodents where noise from movement artifacts can complicate image analysis. Furthermore, SPECT imaging is generally more sensitive to small amounts of tracer than MRI,<sup>63</sup> which makes it suitable for studying small rodents where the tracer volume is limited.

Although SPECT has greater signal sensitivity, the resolution of MRI is superior to SPECT.<sup>64</sup> The large point-spread function of SPECT can also make it difficult to distinguish between small compartments as e.g. the CSF space surrounding the brain and the brain itself (Supplemental Figure 2). This should be kept in mind when designing ROIs for evaluating

tracer influx to the brain, as the signal of large CSF compartments might bleed into areas in close proximity. Because of the lower resolution and larger point-spread function in SPECT, MRI would still be the method of choice for studies of small, defined structures such as cranial nerves or specific brain structures. An exciting possibility is to combine SPECT with other imaging modalities such as MRI or optical imaging, which makes a powerful combination of the high sensitivity of SPECT with high resolution morphological information.<sup>65,66</sup> Such multimodal preclinical scanners have a great potential to expand our current understanding of CSF flow dynamics at the microscopic and even cellular level.

### Outlook and concluding remarks

The SPECT imaging method evaluated here could be used to study disease models of mice and rats, where especially models of neurodegenerative diseases and hypertension, that are both known to be linked to an impaired glymphatic system, would be of great clinical interest. SPECT and PET imaging is already used clinically and experimentally to evaluate amyloid- $\beta$  plaque build-up, a hallmark of Alzheimer's disease.<sup>67–69</sup> A combined imaging of amyloid deposition and glymphatic flow could be used to investigate the link between the glymphatic system and Alzheimer's disease progression. An interesting meta-study would be to use existing clinical data to gain a better understanding of CSF dynamics in humans. There is a wide range of SPECT tracers available, and while radio-ligands binding to specific receptors traditionally have been the most common, radio-ligands for imaging of targets such as tau pathology,<sup>70</sup> apoptosis,<sup>71</sup> and inflammation<sup>72</sup> pave the way for new ways of using SPECT. In conclusion, SPECT/CT is a relevant method for imaging the glymphatic system, and has advantages over MRI in terms of tracer specificity and quantitative signal, which makes it highly suitable for rodent glymphatic imaging.

### Funding

Funding was provided by Lundbeck Foundation grant R386-2021-165, Novo Nordisk Foundation grant NNF20OC 0066419, National Institutes of Health grant R01AT011439, National Institutes of Health grant U19NS128613, US Army Research Office grant MURI W911NF1910280, Human Frontier Science Program grant RGP0036, the Dr. Miriam and Sheldon G. Adelson Medical Research Foundation, and Simons Foundation grant 811237.

### Acknowledgements

We would like to thank Dan Xue for graphic illustrations and the Department of Clinical Physiology, Nuclear Medicine

and PET, Rigshospitalet for providing us with [<sup>99m</sup>Tc] NanoScan tracer.





### Declaration of conflicting interests

The author(s) declared no potential conflicts of interest with respect to the research, authorship, and/or publication of this article.

### Authors' contributions

TOL, SLB, NLH and MN designed the study. TOL, SLB, NLH, KNM, BS, MR, FLHM, LK acquired and analyzed the data. TOL, SLB, NLH, KNM, BS, MP, YM, and FLHM interpreted the data. NLH, BS, NB, FLHM and TOL drafted the manuscript. NLH, TOL, SLB, KNM, BS, FLHM, LK, VS, MH, MP, YM and MN assisted in revising the manuscript and approved the final version.

### ORCID iDs

Björn Sigurdsson  <https://orcid.org/0000-0002-7484-7779>  
 Natalie L Hauglund  <https://orcid.org/0000-0002-2198-6329>  
 Frida L-H Mogensen  <https://orcid.org/0000-0002-3497-2321>  
 Marko P Rosenholm  <https://orcid.org/0000-0002-5437-8282>

### Supplemental material

Supplemental material for this article is available online.

### References

1. Valotassiou V, Malamitsi J, Papatriantafyllou J, et al. SPECT and PET imaging in Alzheimer's disease. *Ann Nucl Med* 2018; 32: 583–593.
2. Guidotti C, Farioli D, Gaeta M, et al. SPECT radiopharmaceuticals for dementia. *Curr Radiopharm* 2014; 6: 192–207.
3. Stone J. Imaging the glutamate system in humans: relevance to drug discovery for schizophrenia. *Curr Pharm Des* 2009; 15: 2594–2602.
4. Kim J-H, Marton J, Ametamey SM, et al. A review of molecular imaging of glutamate receptors. *Molecules* 2020; 25: 4749.
5. van der Vaart MG, Meerwaldt R, Slart RHJA, et al. Application of PET/SPECT imaging in vascular disease. *Eur J Vasc Endovasc Surg* 2008; 35: 507–513.
6. Bockisch A, Freudenberg LS, Schmidt D, et al. Hybrid Imaging by SPECT/CT and PET/CT: Proven Outcomes in Cancer Imaging. *Semin Nucl Med* 2009; 39: 276–289.
7. Benveniste H, Lee H and Volkow ND. The Glymphatic Pathway: Waste Removal from the CNS via Cerebrospinal Fluid Transport. *Neurosci* 2017; 23: 454–465.
8. Iliff JJ, Wang M, Liao Y, et al. A paravascular pathway facilitates CSF flow through the brain parenchyma and the clearance of interstitial solutes, including amyloid. *Sci Transl Med* 2012; 4: 1–11.



9. Yang L, Kress BT, Weber HJ, et al. Evaluating glymphatic pathway function utilizing clinically relevant intrathecal infusion of CSF tracer. *J Transl Med* 2013; 11: 107.
10. Gaberel T, Gakuba C, Goulay R, et al. Impaired glymphatic perfusion after strokes revealed by contrast-enhanced MRI. *Stroke* 2014; 45: 3092–3096.
11. Iliff JJ, Chen MJ, Plog BA, et al. Impairment of glymphatic pathway function promotes tau pathology after traumatic brain injury. *J Neurosci* 2014; 34: 16180–16193.
12. Lee H, Xie L, Yu M, et al. The effect of body posture on brain glymphatic transport. *J Neurosci* 2015; 35: 11034–11044.
13. Huber VJ, Igarashi H, Ueki S, et al. Aquaporin-4 facilitator TGN-073 promotes interstitial fluid circulation within the blood–brain barrier. *Neuroreport* 2018; 29: 697–703.
14. Goulay R, Flament J, Gauberti M, et al. Subarachnoid hemorrhage severely impairs brain parenchymal cerebrospinal fluid circulation in nonhuman primate. *Stroke* 2017; 48: 2301–2305.
15. Ohno K, Samaranch L, Hadaczek P, et al. Kinetics and MR-based monitoring of AAV9 vector delivery into cerebrospinal fluid of nonhuman primates. *Mol Ther Methods Clin Dev* 2019; 13: 47–54.
16. Eide PK and Ringstad G. MRI with intrathecal MRI gadolinium contrast medium administration: a possible method to assess glymphatic function in human brain. *Acta Radiol Open* 2015; 4: 205846011560963.
17. Eide PK, Vatnehol SAS, Emblem KE, et al. Magnetic resonance imaging provides evidence of glymphatic drainage from human brain to cervical lymph nodes. *Sci Rep* 2018; 8: 7194.
18. Ringstad G, Vatnehol SAS and Eide PK. Glymphatic MRI in idiopathic normal pressure hydrocephalus. *Brain* 2017; 140: 2691–2705.
19. Myllylä T, Harju M, Korhonen V, et al. Assessment of the dynamics of human glymphatic system by near-infrared spectroscopy. *J Biophotonics* 2018; 11: 1–9.
20. Fultz NE, Bonmassar G, Setsompop K, et al. Coupled electrophysiological, hemodynamic, and cerebrospinal fluid oscillations in human sleep. *Science* 2019; 366: 628–631.
21. Aspelund A, Antila S, Proulx ST, et al. A dural lymphatic vascular system that drains brain interstitial fluid and macromolecules. *J Exp Med* 2015; 212: 991–999.
22. Jessen NA, Munk ASF, Lundgaard I, et al. The glymphatic system: a beginner's guide. *Neurochem Res* 2015; 40: 2583–2599.
23. Louveau A, Herz J, Alme MN, et al. CNS lymphatic drainage and neuroinflammation are regulated by meningeal lymphatic vasculature. *Nat Neurosci* 2018; 21: 1380–1391.
24. Da Mesquita S, Louveau A, Vaccari A, et al. Functional aspects of meningeal lymphatics in ageing and Alzheimer's disease. *Nature* 2018; 560: 185–191.
25. Du T, Mestre H, Kress BT, et al. Cerebrospinal fluid is a significant fluid source for anoxic cerebral oedema. *Brain* 2022; 145: 787–797.
26. Rasmussen MK, Mestre H and Nedergaard M. Fluid transport in the brain. *Physiol Rev* 2022; 102: 1025–1151.
27. Lundgaard I, Lu ML, Yang E, et al. Glymphatic clearance controls state-dependent changes in brain lactate concentration. *J Cereb Blood Flow Metab* 2017; 37: 2112–2124.
28. Goffin K and van Laere K. Single-photon emission tomography. *Handb Clin Neurol* 2016; 135: 241–250.
29. Giannetto M, Xia M, Stæger FF, et al. Biological sex does not predict glymphatic influx in healthy young, middle aged or old mice. *Sci Rep* 2020; 10: 16073.
30. Xavier ALR, Hauglund NL, Von Holstein-Rathlou S, et al. Cannula implantation into the cisterna magna of rodents. *JoVE* 2018; DOI: 10.3791/57378.
31. Lee H, Mortensen K, Sanggaard S, et al. Quantitative Gd-DOTA uptake from cerebrospinal fluid into rat brain using 3D VFA-SPGR at 9.4T. *Magn Reson Med* 2018; 79: 1568–1578.
32. Avants B, Tustison NJ and Song G. Advanced normalization tools: V1.0. *Insight J* 2009; 2: 1–35.
33. Van den Broeck W, Derore A and Simoens P. Anatomy and nomenclature of murine lymph nodes: Descriptive study and nomenclatory standardization in BALB/cAnNCrl mice. *J Immunol Methods* 2006; 312: 12–19.
34. Mestre H, Du T, Sweeney AM, et al. Cerebrospinal fluid influx drives acute ischemic tissue swelling. *Science* 2020; 367: 1198–1199.
35. Ma Q, Ries M, Decker Y, et al. Rapid lymphatic efflux limits cerebrospinal fluid flow to the brain. *Acta Neuropathol* 2019; 137: 151–165.
36. Hablitz LM, Vinitsky HS, Sun Q, et al. Increased glymphatic influx is correlated with high EEG delta power and low heart rate in mice under anesthesia. *Sci Adv* 2019; 5: 1–8.
37. Xie L, Kang H, Xu Q, et al. Sleep drives metabolite clearance from the adult brain. *Science* 2013; 342: 373–377.
38. Lilius TO, Blomqvist K, Hauglund NL, et al. Dexmedetomidine enhances glymphatic brain delivery of intrathecally administered drugs. *J Control Release* 2019; 304: 29–38.
39. Benveniste H, Lee H, Ding F, et al. Anesthesia with dexmedetomidine and low-dose isoflurane increases solute transport via the glymphatic pathway in rat brain when compared with high-dose isoflurane. *Anesthesiology* 2017; 127: 976–988.
40. Ballinger JR. Radiopharmaceuticals in clinical diagnosis and therapy. In: Khalil MM (Ed.) *Basic sciences of nuclear medicine*. Cham: Springer International Publishing, 2021, pp.103–118.
41. Sarker A, Suh M, Choi Y, et al. [64Cu]Cu-Albumin Clearance Imaging to Evaluate Lymphatic Efflux of Cerebrospinal Space Fluid in Mouse Model. *Nucl Med Mol Imaging (2010)* 2022; 56: 137–146.
42. Iliff JJ, Lee H, Yu M, et al. Brain-wide pathway for waste clearance captured by contrast-enhanced MRI. *J Clin Invest* 2013; 123: 1299–1309.
43. Iida H, Ohata H, Iida M, et al. Isoflurane and sevoflurane induce vasodilation of cerebral vessels via

- ATP-sensitive K<sup>+</sup> channel activation. *Anesthesiology* 1998; 89: 954–960.
44. Ishiyama T, Dohi S, Iida H, et al. Mechanisms of dexmedetomidine-induced cerebrovascular effects in canine in vivo experiments. *Anesth Analg* 1995; 81: 1208–1215.
  45. Bojarskaite L, Bjørnstad DM, Vallet A, et al. Sleep cycle-dependent vascular dynamics enhance perivascular cerebrospinal fluid flow and solute transport. *bioRxiv* 2022. DOI: <https://doi.org/10.1101/2022.07.14.500017>.
  46. Benveniste H, Heerdt PM, Fontes M, et al. Glymphatic system function in relation to anesthesia and sleep states. *Anesth Analg* 2019; 128: 747–758.
  47. Tétrault S, Chever O, Sik A, et al. Opening of the blood-brain barrier during isoflurane anaesthesia. *Eur J Neurosci* 2008; 28: 1330–1341.
  48. Almutairi MMA, Gong C, Xu YG, et al. Factors controlling permeability of the blood–brain barrier. *Cell Mol Life Sci* 2016; 73: 57–77.
  49. Weinmann H, Brasch R, Press W, et al. Characteristics of gadolinium-DTPA complex: a potential NMR contrast agent. *AJR Am J Roentgenol* 1984; 142: 619–624.
  50. Mestre H, Tithof J, Du T, et al. Flow of cerebrospinal fluid is driven by arterial pulsations and is reduced in hypertension. *Nat Commun* 2018; 9: 4878.
  51. Chen X, Liu X, Koundal S, et al. Cerebral amyloid angiopathy is associated with glymphatic transport reduction and time-delayed solute drainage along the neck arteries. *Nat Aging* 2022; 2: 214–223.
  52. Liu G, Mestre H, Sweeney AM, et al. Direct measurement of cerebrospinal fluid production in mice. *Cell Rep* 2020; 33: 108524.
  53. McAfee JG, Gagne G, Atkins HL, et al. Biological distribution and excretion of DTPA labeled with tc-99m and In-111. *J Nucl Med* 1979; 20: 1273–1278.
  54. Howard BA, Gray L, Isaacs RE, et al. Definitive diagnosis of cerebrospinal fluid leak into the pleural space using <sup>111</sup>In-DTPA cisternography. *Clin Nucl Med* 2015; 40: 220–223.
  55. Benveniste H, Lee H, Ozturk B, et al. Glymphatic cerebrospinal fluid and solute transport quantified by MRI and PET imaging. *Neuroscience* 2021; 474: 63–79.
  56. Hablitz LM, Plá V, Giannetto M, et al. Circadian control of brain glymphatic and lymphatic fluid flow. *Nat Commun* 2020; 11: 4411.
  57. Hauglund NL, Kusk P, Kornum BR, et al. Meningeal lymphangiogenesis and enhanced glymphatic activity in mice with chronically implanted EEG electrodes. *J Neurosci* 2020; 40: 2371–2380.
  58. Xue Y, Liu X, Koundal S, et al. In vivo T1 mapping for quantifying glymphatic system transport and cervical lymph node drainage. *Sci Rep* 2020; 10: 14592.
  59. von Holstein-Rathlou S, Petersen NC and Nedergaard M. Voluntary running enhances glymphatic influx in awake behaving, young mice. *Neurosci Lett* 2018; 662: 253–258.
  60. Jiang Q, Zhang L, Ding G, et al. Impairment of glymphatic system after diabetes. *J Cereb Blood Flow Metab* 2017; 37: 1326–1337.
  61. Sweeney AM, Plá V, Du T, et al. In vivo imaging of cerebrospinal fluid transport through the intact mouse skull using fluorescence macroscopy. *J Vis Exp* 2019; 149. DOI: 10.3791/59774.
  62. Streitbürger D-P, Möller HE, Tittgemeyer M, et al. Investigating Structural Brain Changes of Dehydration Using Voxel-Based Morphometry. *PLoS One* 2012; 7: e44195.
  63. Seevinck PR, Seppenwoolde J-H, de Wit TC, et al. Factors affecting the sensitivity and detection limits of MRI, CT, and SPECT for multimodal diagnostic and therapeutic agents. *Anticancer Agents Med Chem* 2007; 7: 317–334.
  64. Meikle SR, Kench P, Kassiou M, et al. Small animal SPECT and its place in the matrix of molecular imaging technologies. *Phys Med Biol* 2005; 50: R45–R61.
  65. Bouziotis P, Psimadas D, Tsotakos T, et al. Radiolabeled iron oxide nanoparticles As dual-modality SPECT/MRI and PET/MRI agents. *Curr Top Med Chem* 2013; 12: 2694–2702.
  66. Culver J, Akers W and Achilefu S. Multimodality molecular imaging with combined optical and SPECT/PET modalities. *J Nucl Med* 2008; 49: 169–172.
  67. Wang Y, Klunk WE, Debnath ML, et al. Development of a PET/SPECT agent for amyloid imaging in Alzheimer's disease. *J Mol Neurosci* 2004; 24: 55–62.
  68. Ferrando R and Damian A. Brain SPECT as a Biomarker of Neurodegeneration in Dementia in the Era of Molecular Imaging: Still a Valid Option? *Front Neurol* 2021; 12. DOI: 10.3389/fneur.2021.629442.
  69. Nguyen GAH, Liang C and Mukherjee J. [124I]IBETA: a new  $\alpha\beta$  plaque positron emission tomography imaging agent for Alzheimer's disease. *Molecules* 2022; 27: 4552.
  70. Yousaf T, Dervenoulas G, Valkimadi P-E, et al. Neuroimaging in Lewy body dementia. *J Neurol* 2019; 266: 1–26.
  71. Luo Q, Zhang Z, Wang F, et al. Preparation, in vitro and in vivo evaluation of <sup>99m</sup>Tc-Annexin B1: A novel radioligand for apoptosis imaging. *Biochem Biophys Res Commun* 2005; 335: 1102–1106.
  72. Meester EJ, Krenning BJ, de Blois RH, et al. Imaging of atherosclerosis, targeting LFA-1 on inflammatory cells with <sup>111</sup>In-DANBIRT. *J Nucl Cardiol* 2019; 26: 1697–1704.